Am J Cancer Res 2026;16(7):2899-2918
www.ajcr.us /ISSN:2156-6976/ajcr0174248

Original Article

Integrating in silico modeling and experimental validation to determine the anti-breast cancer mechanisms of mulberry leaf bioactive compounds

Jun Zhang, Guoxin Zhao, Renping Zhang, Zhengyu Fu, Xinru Chen, Jiong Wu

Zhengzhou University of Technology, Levitt Institute for The Convergence Life Sciences and Digital Technology, 18 Yingcai Street, Zhengzhou 450044, Henan, P. R. China

Received May 23, 2026; Accepted July 2, 2026; Epub July 15, 2026; Published July 30, 2026

Abstract: Breast cancer (BRCA) is the most prevalent malignancy and leading cause of cancer-related death in women. To elucidate the anti-BRCA mechanisms of mulberry leaves (ML), the present study used an integrated strategy combining network pharmacology, molecular docking and in vitro validation. The active components of ML, their putative targets and BRCA-related proteins were screened from public databases (Traditional Chinese Medicine Systems Pharmacology Database and Analysis Platform, and Encyclopedia of Traditional Chinese Medicine). A protein-protein interaction network was constructed using Cytoscape, followed by Gene Ontology (GO) biological function and Kyoto Encyclopedia of Genes and Genes (KEGG) pathway analyses through the Database for Annotation, Visualization and Integrated Discovery. Molecular docking was then conducted to assess the binding affinities of key compounds to prioritized targets. In vitro assays (MTT, wound healing and flow cytometry) were performed to evaluate the effects of ML on MDA-MB-231 cell proliferation, migration, apoptosis and cell cycle progression. Western blotting was conducted to validate core target proteins. In total, nine bioactive ML compounds (such as quercetin and stigmasterol) were identified, targeting six core proteins [tumor protein p53, estrogen receptor 1 (ESR1), catenin β1, AKT serine/threonine kinase 1, MYC proto-oncogene/BHLH transcription factor and telomerase reverse transcriptase]. GO analysis revealed enrichment in 'nucleoplasm', 'enzyme binding' and 'cellular response to hypoxia' terms, whilst KEGG pathway analysis results highlighted 'cancer-related pathways' (such as PI3K/AKT). Stigmasterol exhibited the strongest binding affinity to ESR1 (in silico). In vitro, ML extract significantly suppressed MDA-MB-231 proliferation and migration, induced apoptosis and triggered G_2/M arrest. Western blotting confirmed the downregulation of oncoproteins (TP53, AKT1, ESR1 and JUN). The results of the present study suggest that ML can inhibit the proliferation and migration of BRCA cells whilst inducing their apoptosis by regulating the expression of key proteins. This provides a scientific basis for the in-depth exploration of the anti-BRCA mechanism of ML.

Keywords: Mulberry leaves, breast cancer, in silico, experimental validation, western blotting

Introduction

Breast cancer (BRCA) poses a major global health challenge and is the most prevalent malignancy present among women, accounting for 7-10% of all cases of cancer-related morbidity worldwide [1]. In 2022, there were an estimated 2.31 million new cases of BRCA and BRCA accounted for 670,000 deaths globally, highlighting the notable global disease burden [2]. At present, BRCA is treated with comprehensive treatment methods. Early and mid-term BRCA treatment methods include surgical resection, radiotherapy, chemotherapy, endocrine therapy and molecular targeted therapy [3]. However, current standard therapies for BRCA are often hampered by intrinsic or acquired drug resistance, significant toxic side effects that impair the quality of life of patients, and the challenge of preventing metastasis and recurrence. As reported by Taylor *et al* [4], diet serves an important role in the fighting against cancer, including preventing tumor initiation and responses to therapeutic treatments.

Previous studies have demonstrated that bioactive components in medicinal foods (such as polyphenols in tea or polysaccharides in

https://doi.org/10.62347/PLVO6071

Cordyceps sinensis) can exhibit dual chemopreventative and adjuvant therapeutic effects, through epigenetic modulation and immune potentiation [5, 6]. Cruciferous vegetable-derived sulforaphane has been shown to enhance apoptosis in BRCA cells through nuclear factor erythroid 2-related factor 2 pathway modulation [7]. However, comprehensive clinical validation of dietary interventions is warranted to establish evidence-based guidelines. Mulberry leaves (ML) refer to the leaves of Morus alba L., a species of plants recognized for its dual role as both a medicinal and nutritional resource. Within Traditional Chinese Medicine (TCM), ML have been used for the treatment of blood pressure ailments, respiratory diseases, diabetes mellitus, blindness and hyperpigmentation [8-11]. However, to the best of our knowledge, ML have not been investigated in the context of BRCA and their active compounds, meaning its potential mechanisms are currently unknown.

At present, in silico prediction methods have become a key tool in drug discovery, including network pharmacology, Gene Ontology (GO), Kyoto Encyclopedia of Genes and Genomes (KEGG) and molecular docking strategies [12, 13]. In the present study, an integrated approach of *in silico* analysis and experimental verification was employed to identify the molecular targets of ML and elucidate their anti-BRCA mechanisms. Use of ML not only provided a theoretical basis for their potential use as a daily food ingredient in preventing or treating BRCA but also offered theoretical support for the development of ML-based medications.

Materials and methods

Collection and screening of bioactive compounds in ML

Screening was performed for key components of ML from the published literature [11, 14-16] and related targets from the TCM Systems Pharmacology Database and Analysis Platform (TCMSP; version 2.3; https://tcmsp-e.com/) [17], in addition to The Encyclopedia of TCM Database (ETCM; version 2.0; www.tcmip.cn). From these resources, the association between drugs, targets and diseases, were identified by setting the filter criteria to an oral bioavailability (OB) ≥30% and drug-likeness (DL) ≥0.18. All target proteins were standardized using the UniProt database (UniProt 2023; https://www.uniprot.org/) before gene names, symbols and IDs were elucidated using the GeneCards® database (https://www.genecards.org).

Collection of BRCA-related targets

Targets associated with the key words 'breast cancer' and 'breast tumor' were collected from the Online Mendelian Inheritance in Man (OMIM; https://omim.org/) database and the Human Gene Database within GeneCards®, with a relevance score threshold of >10 applied to filter the GeneCards results. The potential anti-BRCA targets of ML were defined as the intersection between the predicted target genes of ML components and the known BRCA-related disease targets, which was determined using the Venny 2.1.0 online tool (https://bioinfogp.cnb.csic.es/tools/venny/).

Construction and visualization analysis of active components-BRCA-targets network

The online Cytoscape software (version 3.9.0; https://cytoscape.org/) was used for network structure and analysis. In the constructed network, nodes represented the ML, components, targets and disease entities, whilst edges illustrated the interactions among them. Active components were distinguished by variation in shape and color within the network. In the present study, the degree value, defined as the number of direct connections a node has, was used as a topological parameter to assess network influence, with a higher degree value corresponding to greater influence. Accordingly, degree values were calculated using the 'NetworkAnalyzer' plugin within Cytoscape.

Construction and analysis of protein-protein interactions (PPI)

To identify shared targets, a Venn diagram was generated by superimposing potential tumor-interacting and ML-related targets using an online tool created by the Department of Plant Biotechnology and Bioinformatic of Ghent University (http://bioinformatics.psb.ugent.be/) to find collective targets. Targets were imported into the Search Tool for the Retrieval of Interacting Genes/Proteins database (STRING 12.0; http://string-db.org/) and scored for gene

interaction analysis. Organism parameters were set to 'homo sapiens' and the interaction score was set at 0.900 as the minimum cut-off value. To further analyze the PPI network, core genes were screened with topological properties using the 'CytoNCA' plugin within Cytoscape. In total, six parameters, BC, closeness centrality (C-C), degree centrality (DC), eigenvector centrality (EC), local average connectivity (LAC) and network centrality (NC), were selected to calculate the gene score. Genes with a score higher than the median value were obtained. To identify key core genes, the filter process was performed twice.

GO and KEGG enrichment analysis

GO and KEGG enrichment analysis was performed using the Database for Annotation, Visualization and Integrated Discovery (DAVID 2021; https://davidbioinformatics.nih.gov) [18], to elucidate the function of the core genes and evaluate pathways of ML against cancer. The three categories of GO are molecular functions (MF), biochemical pathways (BP) and cellular components (CC). The top 20 enriched GO terms and KEGG pathways were screened and confirmed (false discovery rate <0.05) for further analyses. Visualization of enrichment analysis was performed using the ImageGP online platform (ImageGP 2.0; https://www.bic.ac.cn/ImageGP/). The top 20 terms, filtered based on a *P*-value (corrected) cutoff of <0.01, were plotted through bar graphs or bubble plots.

Molecular docking simulation

Based on the results of network pharmacology, structures of the components in ML were obtained through the ZINC database (https://zinc.docking.org). The crystal structures of the core target proteins, including TP53 (PDB: 1TUP), estrogen receptor 1 (ESR1; PDB: 1A52), catenin β1 (CTNNB1; PDB: 1JDH), AKT1 (PDB: 4EKK), MYC (PDB: 1NKP) and telomerase reverse transcriptase (TERT; PDB: 6D6V), were retrieved from the Protein Data Bank (PDB; http://www.rcsb.org). Before docking studies, proteins have been dehydrated and original ligands have been extracted and stored separately. Molecular docking simulations were then conducted. In the present study, AutoDock Vina (version 1.1.2; http://vina.scripps.edu) was used. The smaller the binding energy, the tighter the binding was deemed [19]. PyMOL software (version 2.5.0; https://pymol.org/) was used for the visualization of components and molecular docking.

Sample preparation of ML

ML was weighed at 50 g using the XPR105/AC electronic balance (Mettler Toledo) and then ground into a fine powder for use in the present study. MLs were purchased from Henan Zhang Zhongjing Pharmacy Co., Ltd. They were immersed in 200 ml 75% ethanol (Shanghai Aladdin Biochemical Technology Co., Ltd.) and underwent ultrasonic treatment in a 90°C water bath for 1 h using the SHA-C thermostatic shaking water bath (Jiangsu Jinyi Instrument Technology Co., Ltd.). Following centrifugation at 10,000×g and 25°C for 20 min using the CH210R high-speed refrigerated centrifuge (Xiangyi Laboratory Instrument Development Co., Ltd.), the supernatant was removed and the pellet was rinsed with an extra 100 ml 75% ethanol. This was followed by a second sonication step in a 90°C water bath for 1 h. The combined supernatant was concentrated to ~20 ml using a rotary evaporator (RE-2000A; Zhengzhou Haiqi Instrument Technology Co., Ltd.) at 30°C under a reduced pressure of <100 Pa, and then lyophilized at -55°C under a vacuum of 15 Pa (achieved with a rotary vane pump) in a freeze-dryer (YTLG-10A; Shanghai Yetuo Technology Co., Ltd.) until completely powdered. The resulting powder was stored at -80°C in a refrigerator for subsequent experimentation.

For dose preparation, sterile conditions were maintained whilst weighing an appropriate amount of ML powder. Analytical grade PBS (Shanghai Aladdin Biochemical Technology Co., Ltd.) was added and the powder was fully dissolved through further vortexing and ultrasonic treatments. The solution was filtered through a 0.22-μm filter and adjusted to the required drug concentration for experimentation. In the present study, the extract, referred to as ML extract (MLE), was used at concentrations of 0, 200, 400, 600, 800 and 1,000 μg/ml.

Cell culture

Human MDA-MB-231 BRCA cells [cat. no. QS-H166; Keycell Biotechnology (Wuhan) Co.,

Ltd.] were taken out of liquid nitrogen storage and cultured in DMEM high glucose complete culture medium (C3060; Shanghai VivaCell Biosciences, Ltd.) containing 10% FBS (FSP500; Shanghai ExCell Biology, Inc.) and 1% penicillin-streptomycin antibiotic solution (SV30010; HyClone; Cytiva). Cells were kept in the NU-5800 humidified incubator (NuAire, Inc.) at 37°C, in a 5% CO_2 environment. All experiments were performed with cells in the logarithmic growth phase.

Cell viability assay

Cells were cultured until they became fully adherent, after which the medium was carefully removed. The wells were then categorized into control and experimental groups. Subsequently, 150 µl MLE (200, 400, 600, 800 and 1,000 µg/ml) was added to the experimental wells, whilst the control wells received an equivalent volume of medium, to evaluate the influence on cell proliferation.

Following incubation periods of 24, 48 and 72 h at 37°C, 20 µl MTT reagent was introduced to each well. Following a further 4 h of incubation at 37°C, the culture medium was aspirated and 150 µl DMSO was added to each well to dissolve the formazan crystals formed. The plate was gently agitated to ensure homogeneous mixing. Finally, the absorbance of each well was measured at 490 nm using the Varioskan LUX multimode microplate reader (Thermo Fisher Scientific, Inc.) to quantify cell viability.

Wound healing assay

Following the aforementioned experimental procedures, cells were organized into three groups (0, 200 and 800 µg/ml) and seeded into a 6-well plate at a density of 2×10^5 cells per well. Once the cells achieved ~90% confluence, a marker was used to delineate a reference line across the base of each well. Subsequently, three uniform wounds were created perpendicular to this line by scratching the cell monolayer with 100-µl sterile pipette tips. To eliminate any detached cells, the wells were carefully rinsed twice with PBS. The cells were then cultured in 2 ml fresh serum-free medium at 37°C. Images of the wounds were captured using the DMI3000 B inverted optical microscope (Leica Microsystems GmbH) at a magnification of ×40 at 0, 24 and 48 h timepoints post-incubation. These images were subsequently analyzed using ImageJ software (version 1.53k; National Institutes of Health) to determine the relative wound width. The migration rate of the cells was assessed by calculating the reduction in wound width over time with the following equation: Cell migration rate = $[(H0-Hn)/H_0]\times100\%$, whereby H_0 is the scratch distance at 0 h and Hn is the scratch distance at 24 or 48 h.

Apoptosis and cell cycle analysis through flow cytometry

Following the aforementioned experimental protocols, MDA-MB-231 cells were categorized and seeded into a 6-well plate for a 48-h cultivation period at 37°C. Cells were then treated with 0.25% trypsin (EDTA-free) for 6 min to detach them from the plate. Following digestion, the cells were centrifuged at 500×g for 4 min and resuspended in PBS, and the supernatant was further centrifuged at 500×g for an additional 3 min (all steps were performed at 4°C). Next, 500 µl binding buffer was introduced to the cell pellet, followed by the addition of 5 µl FITC and 5 µl PI. Annexin V-FITC/PI was purchased from Shanghai Bestbio Biotechnology Co., Ltd. (cat. no. BB-4101). The mixture was vortexed for 8-10 sec using a DLAB vortex mixer (MX-S; DLAB Scientific Co., Ltd.) in a continuous low-speed mode (setting 2 of 6) and incubated at 2-8°C for 30 min before being promptly analyzed for apoptosis using Gallios flow cytometer (Beckman Coulter, Inc.) and Kaluza Analysis Software (version 2.3; Beckman Coulter, Inc.). Following digestion and centrifugation, the cells were fixed in 70% ethanol at 4°C overnight. Following fixation, the cells underwent two rounds of washing with PBS. Subsequently, RNase and PI dye were added and the cells were incubated at 37°C for 30 min to allow for DNA staining. The cell cycle distribution was then assessed using a Gallios flow cytometer (Beckman Coulter, Inc.) and Kaluza Analysis Software (version 2.3; Beckman Coulter, Inc.).

Western blotting

MDA-MB-231 cells were seeded into 60 mm petri dishes and allowed to adhere completely.

They were then randomized into control and treatment groups with varying concentrations (0, 200 and 800 μg/ml) of MLE. Following a 48 h incubation period at 37°C, the cells were collected, rinsed twice with PBS and transferred to a 1 ml centrifuge tube for resuspension. Total protein extraction was conducted on ice using RIPA lysis buffer (cat. no. BF0003; Wuhan Powerful Biology Technology Co., Ltd.) supplemented with PMSF. Protein concentration was determined by a BCA assay. Samples were prepared for analysis by adding an appropriate volume of loading buffer and denaturing at 90°C for 15 min in a water bath.

Using anti-β-actin (cat. no. AC026; ABclonal Biotech Co., Ltd.) as an internal control, the protein samples (20 μg per lane) underwent 10% SDS-PAGE and were subsequently transferred onto a PVDF membrane. The membrane was pre-incubated with 5% skim milk at room temperature for 2 h to block non-specific binding, followed by incubation with the primary antibodies against anti-ESR1 [1:1,000 dilution in TBS containing 1% Tween-20 with 5% FBS (SH30070.01; HyClone™; Cytiva); cat. no. BF0200; Affinity Biosciences], anti-TP53 (1:1,000; cat. no. DF7238; Affinity Biosciences), anti-AKT1 (1:5,000; cat. no. ET1609-47; Huabio) and anti-Jun proto-oncogene (JUN; 1:1,000; cat. no. 24909-1-AF; Proteintech Group, Inc.) at 4°C for 16 h (overnight). After three 10-min washes with TBS with 1% Tween-20, the membrane was incubated with a mixture of HRP-conjugated goat anti-rabbit IgG (H+L) (1:5,000; cat. no. 111-035-003; Jackson ImmunoResearch Laboratories, Inc.) and HRP-conjugated goat anti-mouse IgG (H+L) (1:5,000; cat. no. SA00001-1; Proteintech Group, Inc.) secondary antibodies for 2 h at room temperature. Following incubation with the secondary antibody, the membrane was washed three times (5 min per wash) with TBS with 0.05% Tween-20 buffer (PM0202; Wuhan biodbm Biotechnology Co., Ltd.). The PVDF membrane was developed using an enhanced chemiluminescence detection kit (cat. no. BF0023; Powerful Biology). Band visualization and densitometric analysis were performed using a gel documentation system and ImageJ software 1.52a (National Institutes of Health), respectively.

Statistical analysis

All statistical analyses were performed using GraphPad Prism (version 8.0; Dotmatics). Data were analyzed by one-way ANOVA followed by Dunnett's post hoc test for planned comparisons against the control group. For comparisons of half-maximal inhibitory concentration (IC_{50}) values derived from nonlinear regression, an extra sum-of-squares F test was employed. $P<0.05$ was considered to indicate a statistically significant difference. Each experiment was independently repeated at least three times. Data are presented as the mean ± SD.

Results

Screening of ML bioactive compounds identifying 789 candidates

The initial compilation of 158 ML ingredients was retrieved from TCMSP, a public resource specializing in herb-component-target-disease relationships, supplemented by a comprehensive literature review [17, 20-23]. From the aforementioned 158 ingredients, 60 active ingredients were identified by applying screening criteria based on OB and DL values. After excluding compounds with no active binding targets and duplicated components, 43 active ingredients were obtained (**Table 1**). With addition of the six active compounds extracted from the ETCM, a total of 49 key components were obtained in ML (**Table 1**). Following the identification of the 49 key components, their potential targets were predicted using TCMSP, a process that generated 1,575 ingredient-target pairs. Subsequent removal of duplicates identified a final set of 789 target genes.

BRCA-related targets identified using a Venn diagram

A total of 224 BRCA-related targets were obtained from the GeneCards® database and 824 from the OMIM database. By merging the two datasets and excluding the duplicates, 912 BRCA-related targets were obtained in total. This set was then cross-referenced with the 789 ML-related targets via Venn diagram analysis, identifying 36 overlapping genes as the core putative anti-BRCA targets. These shared targets are shown in **Figure 1** and **Table**

Table 1. OB and DL of 49 active compounds in mulberry leaves

MOLID	Ingredient	OB (%)	DL
MOL000131	EIC	41.9	0.18
MOL001739	Zoomaric acid	35.78	0.19
MOL000098	Quercetin	46.43	0.28
MOL001439	Arachidonic acid	45.57	0.20
MOL000432	Linolenic acid	45.01	1.21
MOL002773	β-carotene	37.18	0.58
MOL000449	Stigmasterol	43.83	0.76
MOL000358	β-sitosterol	36.91	0.75
MOL000675	Oleic acid	33.13	1.18
MOL001771	Poriferast-5-en-3 β-ol	36.91	0.85
MOL002218	Scopolin	56.45	0.39
MOL003840	1'-Methoxy-2'-hydroxydihydromollugin	30.76	0.35
MOL003847	Inophyllum E	38.81	0.85
MOL003849	Isobutyrylmallotochromene	32.8	0.69
MOL003851	Isoramanone	39.97	0.51
MOL003856	Moracin B	55.85	0.23
MOL003857	Moracin C	82.13	0.29
MOL003858	Moracin D	60.93	0.38
MOL003859	Moracin E	56.08	0.38
MOL003860	Moracin F	53.81	0.23
MOL003861	Moracin G	75.78	0.42
MOL003862	Moracin H	74.35	0.51
MOL003879	4-Prenylresveratro	40.54	0.21
MOL000433	FA	68.96	0.71
MOL000729	Oxysanguinarine	46.97	0.87
MOL000057	DIBP	49.63	0.18
MOL000208	(+) -Aromadendrene	55.74	0.18
MOL000263	Oleanolic acid	30.02	0.76
MOL000357	Sitogluside	30.63	0.62
MOL000422	Kaempferol	41.88	0.24
MOL000476	Physician	30.29	0.27
MOL000676	DBP	64.54	0.13
MOL001398	Methyllinolenate	46.15	0.17
MOL001442	phytol	33.82	0.18
MOL003759	Iristectorigenin A	63.36	0.34
MOL003767	Tectorigenin	28.41	0.27
MOL005472	1,2-Benzenedicarboxylicacid,mono(2-ethyl) hexylester	55.17	0.18
MOL006630	Norartocarpetin	54.93	0.24
MOL007179	Linolenic acid ethyl ester	46.10	0.2
MOL007879	Tetramethoxyluteolin	43.68	0.37
MOL011081	Linolenic acid methyl ester	46.15	0.18
MOL013074	6-methoxy-2-oxo-2H-chromen-7-yl-β-D-glucopyranoside	30.05	0.39
MOL013083	Skimmin (8Cl)	38.35	0.32
MOL009312	3'-Caffeoylquinic acid	48.14	0.68
MOL001929	Alexandrin	30.63	0.62
MOL000493	Campesterol	37.58	0.71
MOL000737	Morin	46.23	0.27

MOL001525	Daucosterol	36.91	0.75
MOL006387	Chlorogenic acid	30.58	0.33

MOLID, PyMOL identifier; OB, oral bioavailability; DL, drug-likeness.

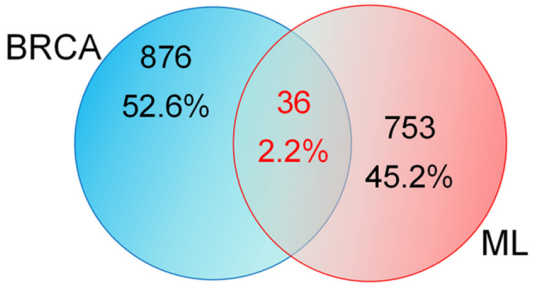

Figure 1. Venn diagram of BRCA- and ML-related targets. BRCA, breast cancer; ML, mulberry leaves.

2. These 36 overlapping targets represented promising core targets for further investigation into the anti-BRCA mechanisms of ML. Consequently, PPI network analysis was conducted on this target set to identify the central hubs within this network.

Construction of active ingredient-BRCA-target network

A visual network map was next established for ML active ingredients and BRCA targets using Cytoscape. Computational inference revealed numerous interactions between active ingredients and key molecular targets, as illustrated in the network (**Figure 2**). The network consists of 87 nodes and 150 edges, with green nodes representing ML, 49 red nodes representing the active components in ML, 36 purple nodes representing tumor/cancer targets and 150 edges representing the interactions among the nodes. The compounds in the network exhibited an average degree value of 3.402, indicating that each compound interacts with 3-4 distinct targets on average, highlighting the multi-component and multi-target interactions associated with BRCA. This implied that the components in ML could be used to manage BRCA, reflected in the multi-component, multi-target and multi-pathway synergy. The 'NetworkAnalyzer' plugin in Cytoscape was used to analyze the component nodes within the network, with key nodes screened based on three topological parameters (BC, C-C and DC). All three parameters were greater than their respective mean values.

Topology analysis of the network revealed an average BC value of 0.0324, an average C-C value of 0.3489 and an average DC value of 16.8776. Further analysis revealed that the BC, C-C and DC values of nine components were greater compared with their corresponding mean values. The nine key active ingredients were identified as quercetin, arachidonic acid, stigmasterol, β-sitosterol, oleic acid, kaempferol, tectorigenin, tetramethoxyluteolin and campesterol (**Table 3**). The present study hypothesized that these nine key active ingredients could be the core components of anti-tumor activity in ML.

PPI network analysis identifies six key proteins

Given that PPI networks are key to a number of biological functions and processes [24] the confidence score of PPI networks can be used to indicate the level of interaction between proteins. A higher score is associated with a greater interaction and a higher level of involvement in biological regulation [25]. Therefore, core targets with a confidence score ≥0.9000 were selected, of which 36 targets were enriched. **Figure 3** shows the network that comprised 36 nodes and 72 edges, with an average node degree of 4, indicating that each node was connected to ~4 others.

Finally, following topological analysis with the six parameters (BC, C-C, DC, EC, LAC and NC) six proteins were identified as key, since their values were greater compared with their respective means of 35.1724, 0.4603, 4.8276, 0.1509, 1.4766 and 2.6761. These proteins were tumor protein p53, ESR1, CTNNB1, AKT1, MYC and TERT (**Table 4**). The larger the BC value, the more likely that BC acts as a 'mediator' and the more important its role in the overall network. The BC value of TP53 reached 235.8111, indicating that it serves an important role in the interactions of ML with BRCA. The second most important protein was CTNNB1, with a BC value of 159.0312. These results suggested that these six genes could be notable targets of BRCA.

Table 2. Formation of potential BC targets from MLs (overlapped targets)

Targets	Official full name	GC ID
TNFRSF1B	TNF receptor superfamily member 1B	GC01P012272
TPR	Translocated promoter region, nuclear basket protein	GC01M186319
TNF	Tumor necrosis factor	GC06P087731
TNFRSF1A	TNF receptor superfamily member 1A	GC12M006328
TP53	Tumor Protein p53	GC17M007661
PRKCA	Protein kinase C α	GC17P066302
PLA2G2A	Phospholipase A2 group IIA	GC01M019975
IL1B	Interleukin 1 β	GC02M112829
CASP8	Caspase 8	GC02P201233
CTNNB1	Catenin β 1	GC03P041236
ADH1B	Alcohol dehydrogenase 1B (Class I), β polypeptide	GC04M099304
IRF1	Interferon regulatory factor 1	GC05M132440
NQO2	N-Ribosyldihydronicotinamide: Quinone reductase 2	GC06P003291
ESR1	Estrogen receptor 1	GC06P151656
PTEN	Phosphatase and tensin homolog	GC10P093576
CCND1	Cyclin D1	GC11P069641
ALDH2	Aldehyde dehydrogenase 2 family member	GC12P111766
AKT1	AKT serine/threonine kinase 1	GC14M104769
NQO1	NAD(P)H quinone dehydrogenase 1	GC16M069706
ERBB2	Erb-B2 receptor tyrosine kinase 2	GC17P039687
MPO	Myeloperoxidase	GC17M058269
CYP2A6	Cytochrome P450 family 2 subfamily A member 6	GC19M040843
BAX	BCL2 associated X, apoptosis regulator	GC19P048954
NCOA3	Nuclear receptor coactivator 3	GC20P047501
CHEK2	Checkpoint kinase 2	GC22M028687
AR	Androgen receptor	GC0XP067544
MED1	Mediator complex subunit 1	GC17M039404
CD40LG	CD40 ligand	GC0XP136649
TERT	Telomerase reverse transcriptase	GC05M001253
CDKN1B	Cyclin dependent kinase inhibitor 1B	GC12P022586
PPARG	Peroxisome proliferator activated receptor γ	GC03P012287
IGF2	Insulin like growth factor 2	GC11M003998
CDK4	Cyclin dependent kinase 4	GC12M057752
MYC	MYC proto-oncogene, BHLH transcription factor	GC08P127735
BCL2	BCL2 apoptosis regulator	GC18M063123
VEGFA	Vascular endothelial growth factor A	GC06P043770

GC ID, GeneCards® identifier.

GO function enrichment analysis

GO function enrichment analysis was performed to further investigate the biological functions of the targets affected by ML in BRCA. Results of the GO enrichment analysis performed on the 36 overlapping target genes yielded a total of 395 entries, including 308 BPs, 31 CCs and 56 MFs. The top 20 most significantly enriched pathways were selected for bubble plot construction (**Figure 4**), which elucidated the mechanisms of ML that can target BRCA.

In the present study, GO BPs were the most significantly enriched. BP results indicated that the targets were mainly associated with 'cellular response to hypoxia', 'positive regulation of

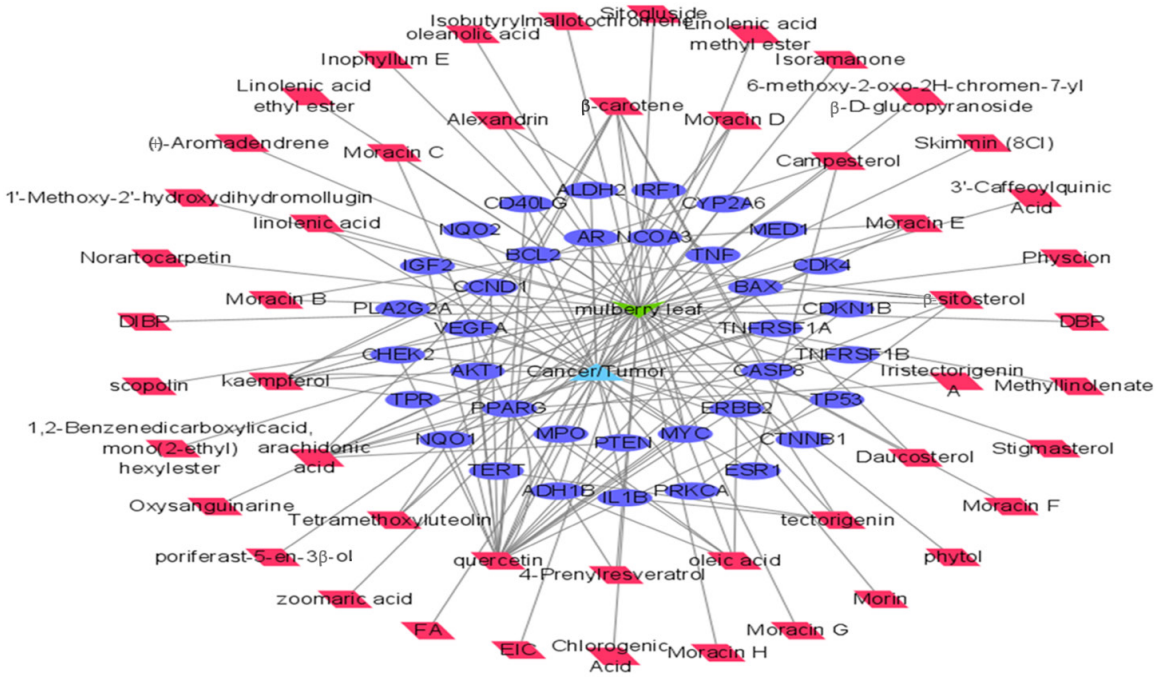

Figure 2. Active ingredient-BRCA-target network. The green label represents ML, blue label represents BRCA, red labels represent active ingredients in ML, purple labels represent targets. BRCA, breast cancer; ML, mulberry leaves.

Table 3. Topological parameters of the core components

MOLID	Key ingredients	BC	C-C	DC
MOL000098	Quercetin	0.4802	0.4699	153.0000
MOL001439	Arachidonic acid	0.1065	0.3637	38.0000
MOL000449	Stigmasterol	0.0538	0.3530	31.0000
MOL000358	β-sitosterol	0.0750	0.3708	38.0000
MOL000675	Oleic acid	0.1581	0.3737	48.0000
MOL000422	Kaempferol	0.1219	0.3888	63.0000
MOL003767	Tectorigenin	0.0682	0.3491	29.0000
MOL007879	Tetramethoxyluteolin	0.0376	0.3530	32.0000
MOL000493	Campesterol	0.1688	0.3550	46.0000

MOLID, PyMOL identifier; BC, betweenness centrality; CC, closeness centrality; DC, degree centrality.

gene expression', 'response to estradiol', 'negative regulation of apoptotic process', 'response to drug', 'positive regulation of transcription from RNA polymerase II promoter', 'intrinsic apoptotic signaling pathway in response to DNA damage' and 'positive regulation of cell proliferation'. CC analysis mainly included 'nucleoplasm', 'macromolecular complex', 'nucleus', 'cytosol', 'cytoplasm', 'chromatin', 'mitochondrion', 'secretory granule' and 'promyelocytic leukemia nuclear body'. For MFs, these targets were mainly associated with 'enzyme binding', 'transcription factor binding', 'identical protein binding', 'chromatin binding', 'protein phosphatase binding', 'protein kinase binding', 'transcription cofactor binding', 'kinase activity', 'transcription coactivator binding' and 'estrogen receptor binding'. The results of this analysis suggest that the anti-BRCA effect of ML was closely associated with the combination of 'nucleoplasm', 'enzyme binding' and 'cellular response to hypoxia'.

KEGG signaling pathway analysis

A total of 162 items were mapped to KEGG signaling pathways, with the top 20 ranked by -log10 *P*-value and presented in **Table 5** as key pathways (**Figure 5** and **Table 5**). Findings suggested that the KEGG pathways of ML were mainly associated with 'pathways in cancer', 'human papillomavirus infection', 'human cytomegalovirus infection', 'hepatocellular carcinoma', 'lipid and atherosclerosis', 'PI3K-AKT signaling pathway', 'endocrine resistance', 'breast

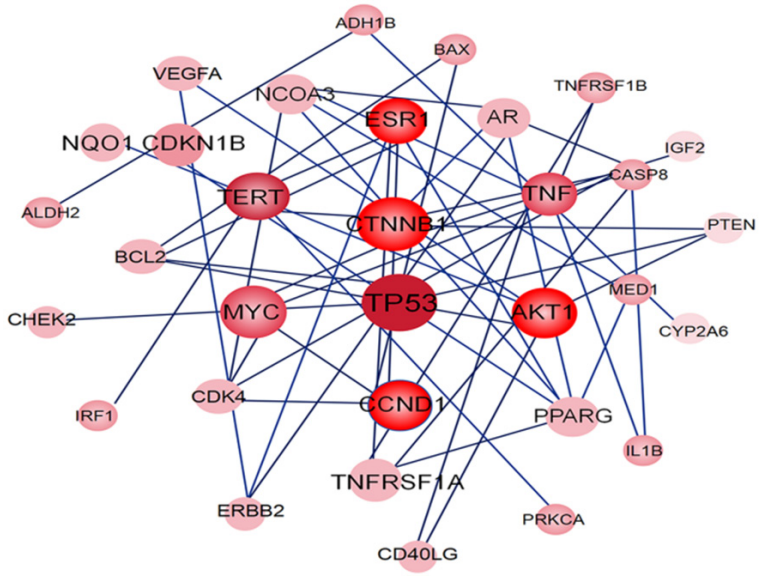

Figure 3. Core targets were obtained using a protein-protein interaction network. ESR1, estrogen receptor 1; CTNNB1, catenin β1; bHLH transcription factor; TERT, telomerase reverse transcriptase.

Table 4. Topological parameters of core targets

Gene	BC	C-C	DC	EC	LAC	NC
TP53	235.8111	0.6222	14.0000	0.3703	2.5714	7.5853
ESR1	66.8116	0.5714	10.0000	0.3442	3.6000	5.9325
CTNNB1	159.0312	0.5714	12.0000	0.3313	2.5000	6.5175
AKT1	73.1861	0.5714	10.0000	0.3324	3.2000	5.4087
MYC	83.9217	0.5957	9.0000	0.3282	3.3333	4.5298
TERT	113.8453	0.5490	8.0000	0.2769	2.7500	3.3571

BC, betweenness centrality; C-C, closeness centrality; DC, degree centrality; EC, eigenvector centrality; LAC, local average connectivity; NC, network centrality; TP53, tumor protein p53; ESR1, estrogen receptor 1; CTNNB1, catenin β1; AKT1, AKT serine/threonine kinase 1; MYC, MYC proto-oncogene, bHLH transcription factor; TERT, telomerase reverse transcriptase.

cancer', 'proteoglycans in cancer' and 'human T-cell leukemia virus 1 infection'. It was therefore hypothesized that ML may exert anti-BRCA effects by regulating these aforementioned signaling pathways.

Molecular docking interactions

Molecular docking was used to evaluate interactions between components of ML and core targets in BRCA. Proteins with the highest values in the PPI network (**Figure 3**), namely TP53 (PDB: 1TUP), ESR1 (PDB: 1A52), CTNNB1 (PDB: 1JDH), AKT1 (PDB: 4EKK), MYC (PDB: 1NKP) and TERT (PDB: 6D6V), which were retrieved from the Research Collaboratory for Structural Bioinformatics PDB database, were used as receptors for molecular docking. The nine compounds, quercetin, arachidonic acid, stigmasterol, β-sitosterol, oleic acid, kaempferol, tectorigenin, tetramethoxyluteolin and campesterol, were used as prospective ligands for molecular docking studies. A lower binding energy between a component and its target indicated a stronger interaction, suggesting that the active ingredient bound more tightly to the target site. For the present study, a binding energy of <-4.25 kcal/mol indicated that the ligand can spontaneously interact with the receptor. Values of <-5.0 kcal/mol suggested good binding activity, while those of <-7.0 kcal/mol reflected a strong binding affinity [25, 26].

As shown in **Table 6**, the lowest binding energy was selected for molecular docking with the ligand and receptor, namely TP53 and stigmasterol (-7.9 kcal/mol), ESR1 and stigmasterol (-10.0 kcal/mol), CTNNB1 and kaempferol (-7.3 kcal/mol), AKT1 and tectorigenin, campesterol (-6.5 kcal/mol), MYC and stigmasterol (-5.7 kcal/mol) as well as TERT and tetramethoxyluteolin (-7.1 kcal/mol). Amongst these, the binding energy of ESR1 to stigmasterol was the lowest, at -10.0 kcal/mol.

Following ligand and receptor docking, a 3D model was generated. As illustrated in **Figure 6**, each ligand specifically bound to functionally critical domains of its respective protein target through multi-modal interactions dominated by hydrogen bonding. Kaempferol localized deep in the CTNNB1 armadillo repeat domain, forming a dense hydrogen-bond network with residues, including THR-205, ARG-200 and ASN-161, while campesterol engaged the AKT1 kinase domain near the ATP-binding site

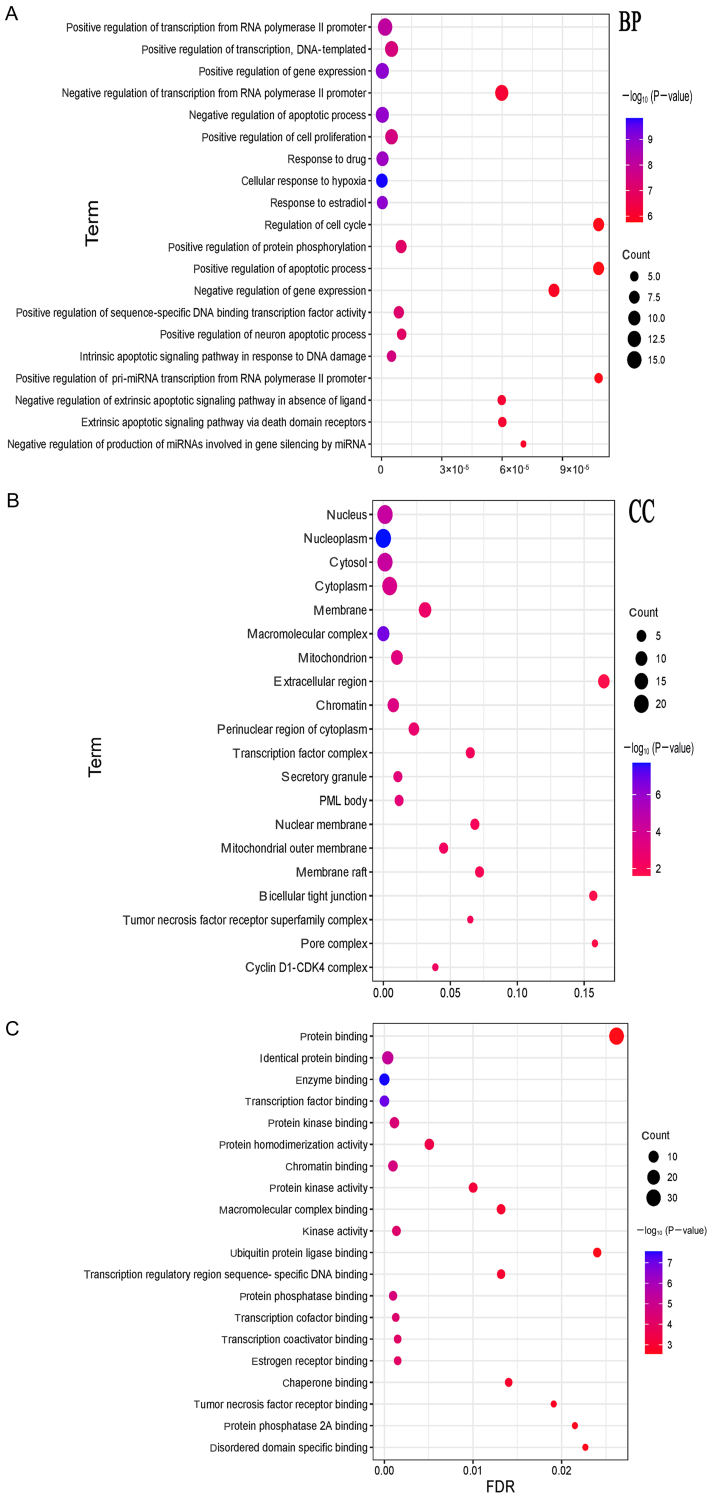

Figure 4. GO functional enrichment analysis. Bubble plot y-axis demonstrates the top 20 significantly enriched (A) BP, (B) CC and (C) MF categories. X-axis shows the number of enriched genes for these terms (FDR<0.01). Color scales represent *P*-value ranges (darker red, higher significance). Bubble size corresponds to the count of the associated genes. GO, gene ontology; BP, biological process; CC, cellular component; MF, molecular function; PML, promyelocytic leukemia nuclear; miRNA; microRNA; FDR, false discovery rate.

via interactions with GLU-91 and HIS-13. Stigmasterol exhibited distinct binding modes across targets: In ESR1, it formed a salt bridge with ARG-394 in the ligand-binding domain; in MYC, it bound the basic helix-loop-helix domain near ARG-65; and in TP53, it interacted with HIS-179. Tetramethoxyluteolin occupied the TERT binding pocket, forming dual hydrogen bonds with TYR-1010 and ARG-972. The consistently low binding energies (≤-7.0 kcal/mol) arose from complementary electrostatic surfaces, optimal burial of hydrophobic moieties and extensive charge stabilization within deep binding clefts [13]. These interactions predict functionally consequential effects, including allosteric inhibition of CTNNB1 transcriptional activity, obstruction of AKT1 phosphorylation and disruption of ESR1-mediated transcription, collectively supporting the anti-BRCA efficacy predicted by network pharmacology [20, 25].

MLE inhibits the viability of MDA-MB-231 cells

The results of the aforementioned network pharmacology and molecular docking studies suggested that ML have a notable inhibitory effect on BRCA. However, to the best of our knowledge, systematic research on the inhibition of BRCA by ML remains poorly understood. To clarify the effect of ML on MDA-MB-231 BRCA cells, MLE was prepared and an MTT assay was conducted to investigate the effect of different MLE concentrations on the proliferation and viability of the MDA-MB-231 cells.

As illustrated in **Figure 7**, MLE demonstrated a notable dose- and time-dependent inhibitory effect on MDA-MB-231 cells, evidenced by both the progressive decline in cell viability with increasing concentration or prolonged exposure

Table 5. Top 20 KEGG enriched pathways

Term	Name	Count	*P*-value	Gene symbols
hsa05200	Pathways in cancer	22	3.28×10^{-17}	NQO1, CDKN1B, NCOA3, PTEN, IGF2, PRKCA, ESR1, VEGFA, AR, CASP8, TERT, CCND1, CDK4, MYC, TPR, ERBB2, BCL2, BAX, AKT1, CTNNB1, PPARG and TP53
hsa05165	Human papillomavirus infection	14	2.72×10^{-10}	CDKN1B, PTEN, TNF, TNFRSF1A, VEGFA, CASP8, TERT, CCND1, CDK4, IRF1, BAX, AKT1, CTNNB1 and TP53
hsa05163	Human cytomegalovirus infection	13	4.60×10^{-11}	PRKCA, TNF, TNFRSF1A, VEGFA, CASP8, CCND1, CDK4, MYC, IL1B, BAX, AKT1, CTNNB1 and TP53
hsa05225	Hepatocellular carcinoma	12	3.84×10^{-11}	NQO1, CCND1, TERT, CDK4, MYC, PTEN, IGF2, BAX, CTNNB1, AKT1, PRKCA and TP53
hsa05417	Lipid and atherosclerosis	12	5.50×10^{-10}	CYP2A6, CASP8, CD40LG, IL1B, BCL2, BAX, AKT1, PRKCA, PPARG, TNF, TP53 and TNFRSF1A
hsa04151	PI3K-AKT signaling pathway	12	1.02×10^{-7}	CDKN1B, CCND1, CDK4, MYC, ERBB2, PTEN, BCL2, IGF2, AKT1, PRKCA, TP53 and VEGFA
hsa01522	Endocrine resistance	11	4.02×10^{-12}	MED1, CDKN1B, CCND1, CDK4, NCOA3, ERBB2, BCL2, BAX, AKT1, ESR1 and TP53

KEGG, Kyoto Encyclopedia of Genes and Genomes; TP53, tumor protein p53; ESR1, estrogen receptor 1; CTNNB1, catenin β1; AKT1, AKT serine/threonine kinase 1; MYC, MYC proto-oncogene, bHLH transcription factor; TERT, telomerase reverse transcriptase.

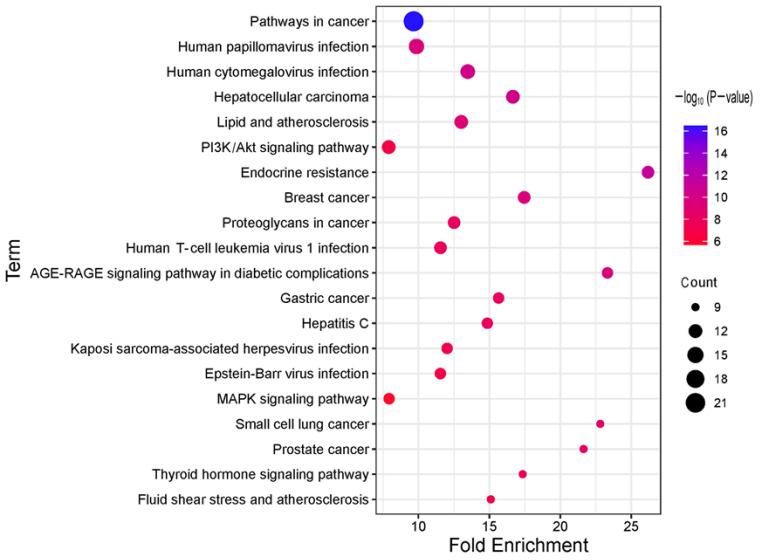

Figure 5. Enrichment analysis of KEGG signaling pathway. Colors indicate different *P*-value ranges, as the redder the bubble, the more significantly enriched the term is. Bubble size is associated with the number of related genes. KEGG, Kyoto Encyclopedia of Genes and Genomes.

and the marked decrease in IC_{50} from 586.5 μg/ml at 24 h to 138.4 μg/ml at 72 h, indicating cumulative and irreversible cellular damage. Based on this enhanced efficacy at 72 h, two concentrations, 200 μg/ml (near the IC_{50}, inducing a critical transition in cell fate with viability <40%) and 800 μg/ml (well above the IC_{50}, triggering thorough execution of death pathways with viability <20%), were selected to dissect the mechanisms underlying the action of MLE across distinct biological endpoints.

MLE suppresses the migratory ability of MDA-MB-231 cells

Following treatment with different concentrations of MLE (0, 200 and 800 μg/ml), the lateral migration ability of MDA-MB-231 cells was found to be significantly inhibited (**Figure 8A**). When cultured for 24 h, the migration rates of MDA-MB-231 cells in the experimental groups with concentrations of 200 μg/ml and 800 μg/ml were 22.14 and 15.98%, respectively. These values were significantly lower compared with those in the control group. When cultured for 48 h, the migration abilities of the two groups exhibited more pronounced inhibitory effects, compared with those in the control group (**Figure 8B**). The present study suggested that MLE has the capacity to impede the motility of MDA-MB-231 cells and inhibit their proliferation. Furthermore, this effect exhibited dose-time dependence.

Table 6. Energy scores of molecular docking between receptors and ligands

Key component	Docking score					
	TP53	ESR1	CTNNB1	AKT1	MYC	TERT
Quercetin	-7.8	-8.1	-7.1	-6.1	-5.3	-6.7
Arachidonic acid	-4.3	-5.7	-4.6	-3.5	-3.3	-4.6
Stigmasterol	-7.9	-10.0	-6.7	-6.3	-5.7	-6.8
β-sitosterol	-6.9	-9.2	-6.9	-6.1	-5.0	-5.9
Oleic acid	-4.4	-5.2	-4.0	-3.4	-2.8	-4.0
Kaempferol	-7.2	-8.1	-7.3	-6.3	-5.0	-6.8
Tectorigenin	-7.2	-7.6	-6.6	-6.5	-5.2	-6.5
Tetramethoxyluteolin	-6.7	-7.2	-6.4	-6.4	-5.3	-7.1
Campesterol	-7.4	-9.2	-6.5	-6.5	-5.2	-6.3

TP53, tumor protein p53; ESR1, estrogen receptor 1; CTNNB1, catenin β1; AKT1, AKT serine/threonine kinase 1; MYC, MYC proto-oncogene, bHLH transcription factor; TERT, telomerase reverse transcriptase.

MLE induces cell cycle G_2/M arrest in MDA-MB-231 cells

Flow cytometry analysis demonstrated that the exposure of MDA-MB-231 cells to MLE at concentrations of 200 and 800 μg/ml for 24 h resulted in dose-dependent cell cycle perturbations compared with those in the untreated control (**Figure 9A**). Specifically, the proportions of cells in both the G_0/G_1 and S phases were significantly reduced, whereas the G_2/M phase population was significantly increased (**Figure 9B**). The associated decline in the S phase fraction with escalating MLE concentrations further indicated cell cycle suppression. Notably, the accumulation of G_2/M phase cells implied an MLE-induced G_2/M arrest, which perhaps disrupted mitotic progression.

MLE induces concentration-dependent apoptosis in MDA-MB-231 cells

Flow cytometry analysis revealed that treatment with MLE at concentrations of 200 and 800 μg/ml significantly increased the apoptotic rate of MDA-MB-231 cells, as compared with the untreated control group (**Figure 10**). As shown in **Figure 10A**, MLE treatment induced a dose-dependent shift of the cell population from the viable region to the early apoptotic quadrant (Annexin V+/PI-), with further progression to the late apoptotic quadrant at higher concentrations. The apoptosis index increased dose-dependently, with early apoptotic cells (Annexin V+/PI-) constituting the predominant population (**Figure 10B**). Notably, no significant changes were observed in the Q1 quadrant (Annexin V-/PI+), ruling out necrosis as a key contributor. MLE treatment induced a dose-dependent increase in both early and late apoptotic cell populations, while no significant necrotic population was observed even at the highest concentration (800 μg/ml). This clear progression through the canonical apoptotic pathway, without prominent necrosis, confirmed that MLE selectively induced apoptosis rather than non-specific cytotoxicity. This pro-apoptotic effect aligned with earlier findings on MLE-induced cell cycle arrest and DNA damage responses.

MLE downregulates the expression of key BRCA proteins in MDA-MB-231 cells

Integrated network pharmacology and molecular docking analyses identified TP53, AKT1, ESR1 and JUN as core targets mediating the anti-BRCA effects of ML. Although CTNNB1 was identified as a potential target, the protein expression of JUN, a canonical downstream transcriptional effector of the CTNNB1/T-cell factor complex, was assessed to evaluate MLE-induced inhibition of the pathway [27]. This approach provides a more functional readout of pathway activity than measuring CTNNB1 levels alone, as JUN expression directly reflects the transcriptional output of the pathway. Furthermore, in the MDA-MB-231 cell model, where Wnt/CTNNB1 signalling is often constitutively activated intracellularly, targeting and assessing the core downstream node linking CTNNB1 to JUN offers a definitive strategy to validate the network pharmacology predictions [28, 29]. Subsequent western blotting confirmed that MLE significantly modulated the expression levels of these key regulatory proteins (**Figure 11A**).

Western blotting demonstrated that MLE treatment at concentrations of 200 and 800 μg/ml significantly downregulated critical oncogenic regulators in MDA-MB-231 cells, including ESR1, AKT1, TP53 and JUN. The inhibitory effects exhibited dose dependency, with the

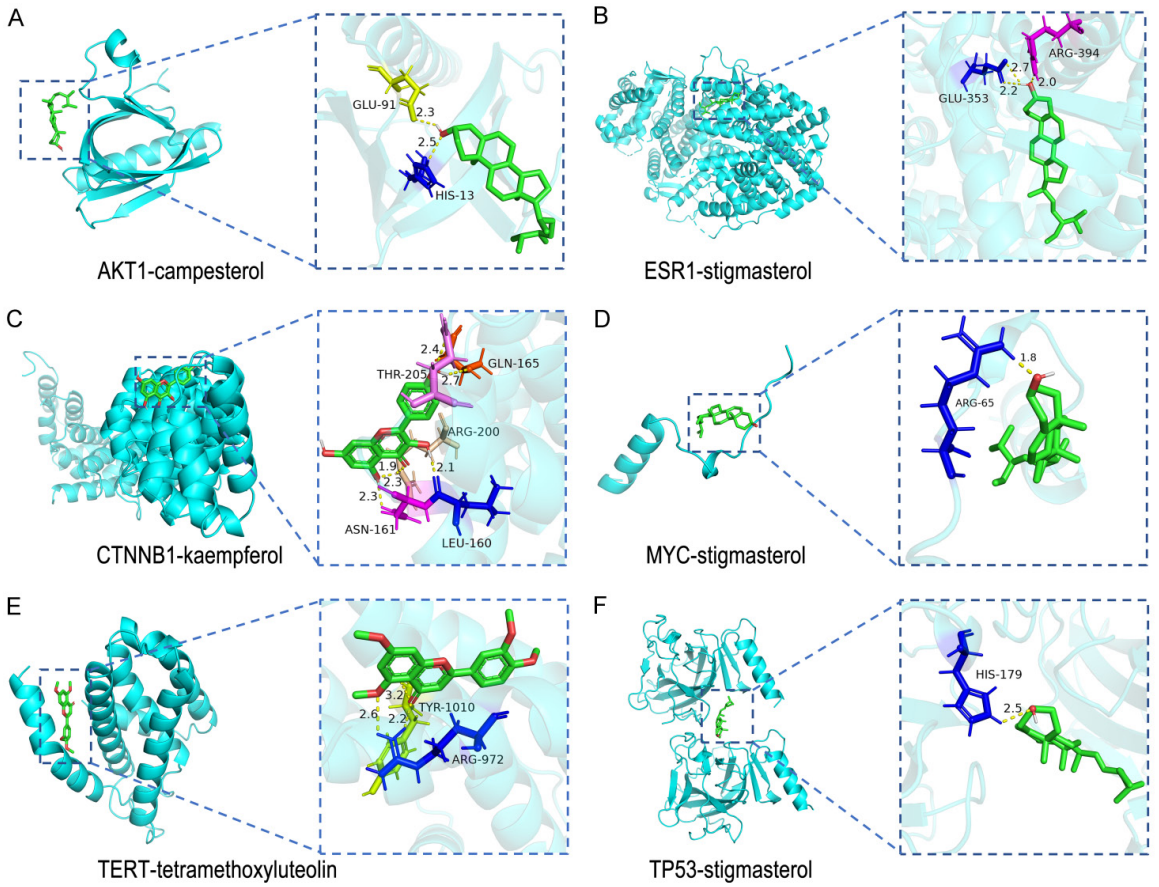

Figure 6. Molecular view of the best docking complexes between the ingredients and potential targets. The three-dimensional structures of the proteins are shown in cyan. The bound ligands are depicted as green sticks. Insets provide detailed views of the specific molecular interactions between the ligands and the amino acid residues within the binding pockets. Yellow dashed lines represent hydrogen bonds, with the corresponding distances labelled in Å. A. AKT1-campesterol: Campesterol forms hydrogen bonds (2.3 and 2.5 Å) with key residues GLU-91 and HIS-13 in the kinase domain of AKT1. B. ESR1-stigmasterol: Stigmasterol binds within the ligand-binding domain of ESR1, forming strong hydrogen bonds with residues GLU-353 (2.7 and 2.2 Å) and ARG-394 (2.0 Å). C. CTNNB1-kaempferol: Kaempferol engages in an extensive hydrogen bond network with residues including ASN-161, GLN-165, ARG-200 and THR-205 (distances ranging between 1.9 and 2.7 Å) on the surface of CTNNB1. D. MYC-stigmasterol: Stigmasterol interacts with the MYC protein via a short hydrogen bond (1.8 Å) with residue ARG-65, suggesting a high-affinity interaction. E. TERT-tetramethoxyluteolin: Tetramethoxyluteolin binds to the TERT protein, forming hydrogen bonds with TYR-1010 (2.6 Å) and ARG-972 (2.2 Å). A distance of 3.2 Å suggests a potential π-π or hydrophobic interaction. F. TP53-stigmasterol: Stigmasterol was shown to form a hydrogen bond (2.5 Å) with residue HIS-179. ESR1, estrogen receptor 1; CTNNB1, catenin β1; TERT, telomerase reverse transcriptase.

800 μg/ml dose achieving a >50% reduction in protein expression levels compared with those in untreated cells (**Figure 11B**). Notably, these targets were consistent with the network pharmacology predictions in the present study, functionally implicating the PI3K/AKT signaling axis and p53-mediated apoptotic pathways as key mechanisms underlying the antitumor activity of MLE.

Discussion

BRCA is a common and highly lethal malignancy affecting women. The search for effective natural anti-cancer agents has become an important direction for current research. The present study used an integrated strategy combining network pharmacology, molecular docking and in vitro experiments to systematically explore the anti-BRCA mechanisms of ML. Key findings from the present *in silico* modeling revealed a multi-component, multi-target mechanistic model for ML, wherein nine bioactive constituents (quercetin, arachidonic acid, stigmasterol, β-sitosterol, oleic acid, kaempferol, tectorigenin, tetramethoxyluteolin and campesterol) collectively targeted a core network of six proteins (TP53, ESR1, CTNNB1, AKT1, MYC

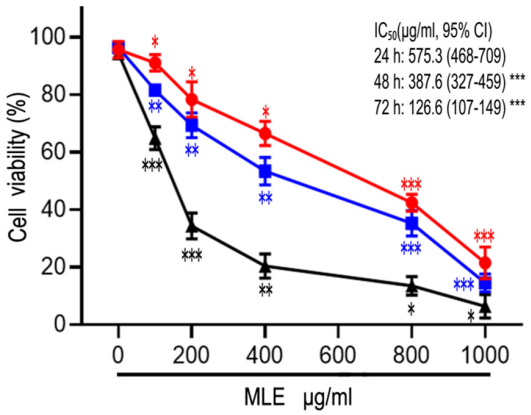

Figure 7. Time- and dose-dependent cytotoxic effects of MLE on MDA-MB-231 cell viability. Cells were treated with increasing concentrations of MLE (0-1,000 μg/ml) for 24, 48 and 72 h. Cell viability was assessed using an MTT assay and is expressed as a percentage. Data are presented as the mean ± SD (n=3). Within each time group, significant differences from the control (0 μg/ml) were determined by one-way ANOVA followed by Dunnett's post hoc test (*P<0.05, **P<0.01, ***P<0.001). Dose-response curves were fitted using a three-parameter nonlinear regression model (top plateau constrained to 100%) to determine the IC_{50} and its 95% CI, from which the overall difference in IC_{50} across time points was evaluated by an extra sum-of-squares F test (P<0.0001). Based on this global significance and non-overlapping 95% CIs, the IC_{50} values at 48 and 72 h were significantly lower than those at 24 h (***P<0.001). This conclusion is supported by the extremely significant result of the extra sum-of-squares F test (P<0.0001) and the widely non-overlapping 95% confidence intervals, which together provide strong evidence for a *P*-value of less than 0.001. MLE, mulberry leaf extract.

and TERT) to exert anticancer effects. These interactions regulated key biological processes, such as 'nucleoplasm' localization, 'enzyme binding' and 'cellular response to hypoxia' and are enriched in various cancer-related pathways, such as PI3K/AKT. Notably, molecular docking analysis demonstrated that stigmasterol exhibited the strongest binding affinity to ESR1 among all components, forming specific hydrogen bonds with key residues, including ARG-394 and GLU-353. Consistent with these computational findings, *in vitro* assays confirmed that MLE significantly suppressed proliferation and migration, induced apoptosis and triggered G_2/M phase cell cycle arrest in MDA-MB-231 cells. These antitumor effects were accompanied by the modulation of key oncoproteins (such as TP53 and ESR1) implicated in BRCA progression. Collectively, these results established a multi-component (for example, quercetin and kaempferol), multi-target (for example, AKT1, TP53 and JUN) and multi-pathway (for example, PI3K-AKT signalling and p53 signalling) framework for the anti-BRCA activity of ML, bridging computational predictions and experimental validation.

The anti-cancer potential of natural products derived from ML has been previously suggested, with studies demonstrating their inhibitory effects on human BRCA and colon cancer cell lines [30-32]. Consistent with these findings, the present in vitro data demonstrated that MLE effectively suppressed MDA-MB-231 cell viability and migration, reinforcing the role of ML as a promising source of anti-tumor agents. However, previous studies regarding ML-derived compounds have only focused on single components or isolated pathways, such as lectin [30] and the inducible nitric oxide synthase-dependent oxidative stress pathway [31], lacking a systematic understanding of their holistic mechanisms. The present study addressed this by leveraging network pharmacology to identify nine bioactive components and six core targets, revealing a complex regulatory network that extends beyond individual molecules to systemic pathway modulation. Whilst the anti-BRCA activity of quercetin has previously been reported [33], the present study contextualized it within a broader framework involving ESR1, AKT1 and PI3K/AKT signaling, therefore providing a more comprehensive view of its therapeutic potential.

Notably, the identification of stigmasterol as a high-affinity ligand for ESR1 in the present study is an important finding [33]. ESR1 is a well-established therapeutic target in BRCA, particularly in estrogen receptor positive (ER+) subtypes [34]. However, its role in triple-negative BRCA cells, such as MDA-MB-231, has not been explored in detail.

The finding that stigmasterol binds to ESR1 with strong affinity suggested a potential non-canonical role for ESR1 in triple-negative BRCA or alternatively, a mechanism through which ML components modulate ESR1-related pathways independently of estrogen signaling. This supports the notion of ESR1 as a context-dependent therapeutic target in BRCA, consistent with previous studies highlighting its role across BRCA subtypes [35-38].

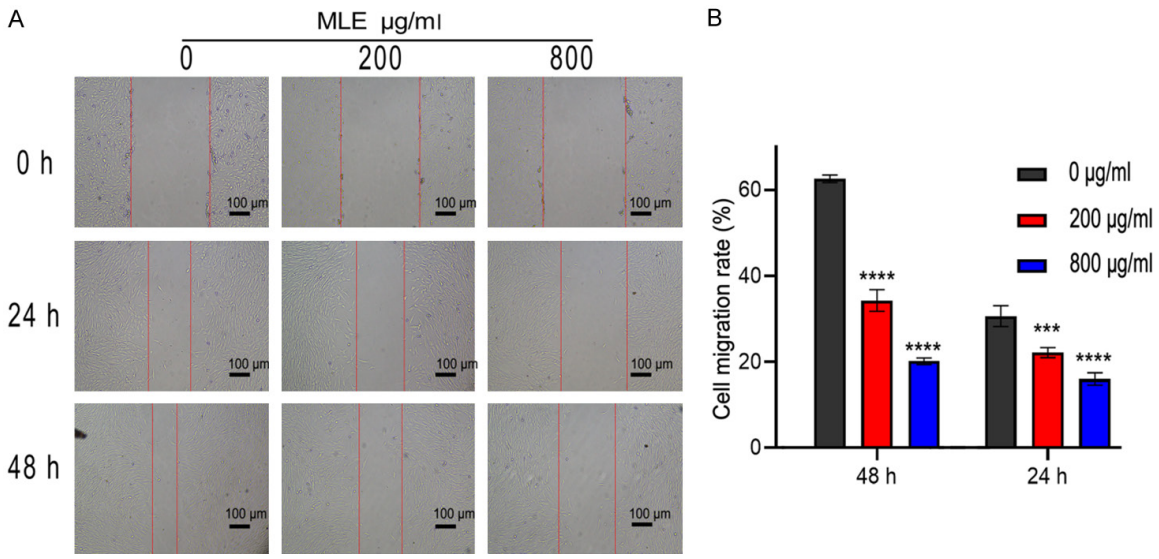

Figure 8. Effect of MLE on the migration ability of MDA-MB-231 breast cancer cells. A. A wound healing assay was performed to detect the migration ability of cells (magnification, ×40) in the blank control, low MLE concentration (200 μg/ml) and high MLE concentration (800 μg/ml) groups. The scratch was observed at 0, 24 and 48 h time-points. B. The healing rate of the wounds was statistically analyzed. The experiment was repeated three times. ***P<0.001, ****P<0.0001 vs. control group. MLE, mulberry leaf extract.

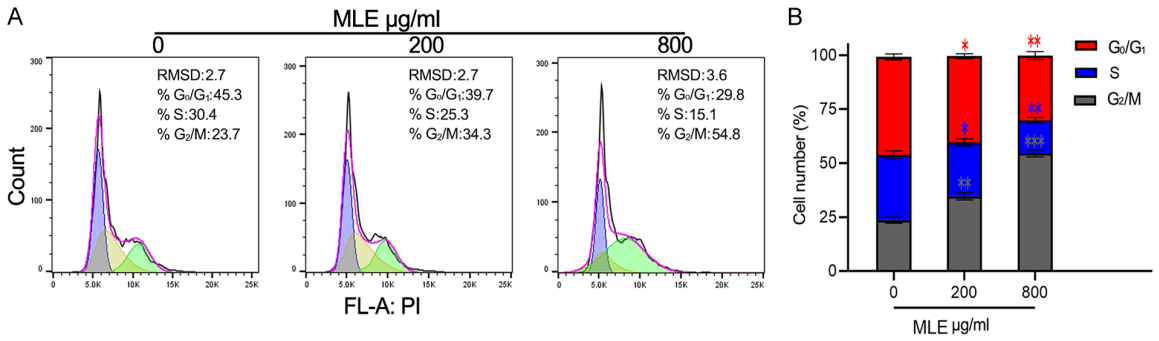

Figure 9. Effect of MLE on the cell cycle of breast cancer MDA-MB-231 cells. A. Effect of MLE on cell cycle distribution through flow cytometry analysis. The x-axis shows the fluorescence intensity of PI staining, quantified as the signal in the FL-A channel, and the y-axis represents the cell count. The RMSD serves as a metric for the goodness-of-fit in cell cycle analysis. B. Cell cycle distribution of MDA-MB-231 cells after treatment with the indicated concentrations of MLE. Statistical significance was determined by one-way ANOVA followed by Dunnett's post hoc test, comparing each MLE-treated group to the untreated control (0 μg/ml) within the same cell cycle phase. *P<0.05, **P<0.01, ***P<0.001 vs. control group. FL-A, fluorescence channel A; MLE, mulberry leaf extract; RMSD, root mean square deviation.

The mechanistic framework uncovered in the present study may exhibit theoretical and practical relevance. Theoretically, it exemplifies how network pharmacology can decode the 'multi-component, multi-target' complexity of natural products, addressing a long-standing challenge in herbal medicine research [39, 40]. In addition, by linking specific ML bioactive components to key cancer-related proteins (such as TP53 and AKT1), the molecular mechanism underlying the anti-tumor effects of ML has been evaluated. In addition, the ability of MLE to induce G_2/M cell cycle arrest and apoptosis in MDA-MB-231 cells underscores its potential as a complementary therapy for triple-negative BRCA.

A number of limitations of the present study should be acknowledged. In vitro experiments focused solely on the MDA-MB-231 cell line.

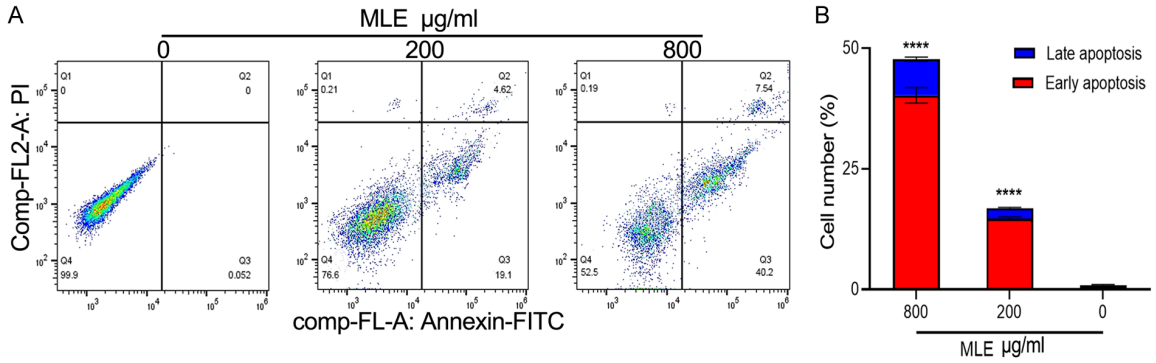

Figure 10. Effect of MLE on MDA-MB-231 apoptosis. A. Effect of MLE on apoptosis distribution by flow cytometry. The x-axis shows compensated Annexin V-FITC fluorescence (an early apoptotic marker), and the y-axis shows compensated PI fluorescence (a marker for late apoptosis/necrosis); FITC and PI are two distinct fluorescent dyes; and FL-A and FL2-A designate the specific optical paths (fluorescence channels) of the flow cytometer. B. Bar graph of cell death in MDA-MB-231 cells (n=3; ****P<0.0001 vs. blank control group). Comp, compensated; FL-A, fluorescence channel A; MLE, mulberry leaf extract.

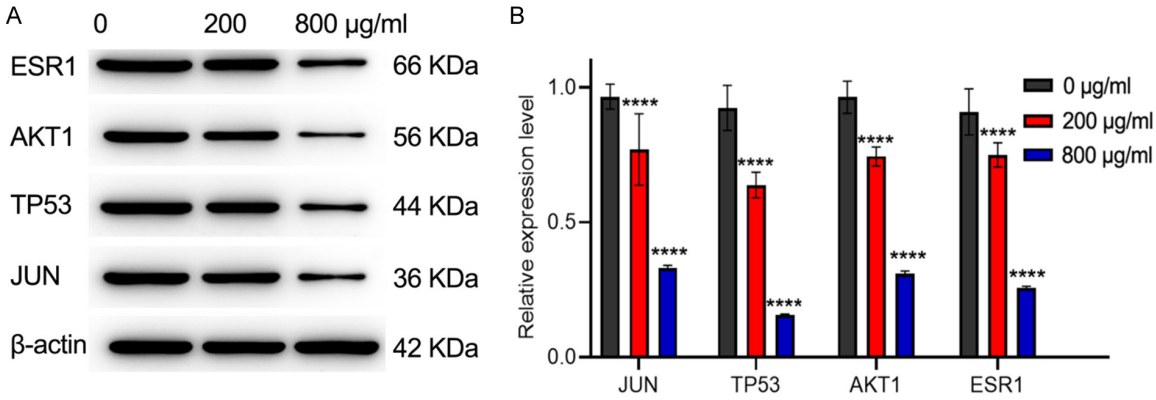

Figure 11. Effect of mulberry leaf extract on the expression of key target proteins in MDA-MB-231 cells. A. Representative bands of key targets in MDA-MB-231 cells, as measured by western blotting. B. Bar graph of the expression levels of key targets in MDA-MB-231 cells (n=3; ****P<0.0001 vs. blank control group). ESR1, estrogen receptor 1; CTNNB1, catenin β1.

Therefore, validation in other BRCA subtypes (such as ER+ MCF-7 and HER2+ SKBR3 lines) is needed to generalize the anti-tumor spectrum of ML. Although network pharmacology successfully identified nine bioactive components in MLE, the individual contributions of these components to the overall pharmacological effects of MLE remain unassessed. Molecular docking analysis provided static binding affinities, but dynamic interactions (perhaps through molecular dynamics simulations) could more accurately reflect the stability of stigmasterol and ESR1 or quercetin and AKT1 complexes in physiological conditions. Finally, in vivo studies to confirm the anti-tumor efficacy of MLE in animal models are lacking, which is key in evaluating pharmacokinetics (such as bioavailability) and potential toxicity.

Therefore, future research should build on the present findings to advance translational relevance. In vivo studies utilizing BRCA xenograft models (including triple-negative BRCA models) are key to validate the anti-tumor efficacy of MLE and establish physiologically relevant dosing regimens. These experiments should aim to employ a refined concentration range (0.1-10 μg/ml), guided by pharmacokinetic profiling and incorporate fractionated extracts to isolate and evaluate the contributions of specific bioactive subcomponents. In addition, functional studies of individual components (such as stigmasterol or quercetin) should aim to clarify their specific roles in regulating ESR1, AKT1 and downstream pathways. This could inform the development of purified ML-derived agents with enhanced potency. Combination

studies with standard-of-care therapies (such as chemotherapy or PI3K inhibitors) should also be performed to explore synergistic effects to reduce drug resistance. Clinical trials evaluating the safety of MLE safety and efficacy in BRCA patients could pave the way for its integration into complementary medicine regimens in the future.

In summary, the present study integrated computational and experimental approaches to elucidate the multi-target mechanisms by which ML acts against BRCA, identifying its key bioactive constituents and associated targets. These findings deepened the mechanistic insights into the efficacy of ML and strengthen its potential for translation. The constructed target-pathway network provides a foundation for developing ML-derived therapeutics, guides compound screening and may support rational combination strategies with conventional chemotherapy to improve efficacy or overcome resistance. The present study bridged predictive modeling with biological validation, accelerating the translation of ML from traditional use toward evidence-based anti-BRCA applications.

Acknowledgements

The present study was supported by the High-level Talent Research Projects of Zhengzhou University of Technology (500-22077), and construct program of the key discipline in Zhengzhou University of Technology.

Disclosure of conflict of interest

None.

Address correspondence to: Jiong Wu, Zhengzhou University of Technology, Levitt Institute for The Convergence Life Sciences and Digital Technology, 18 Yingcai Street, Zhengzhou 450044, Henan, P. R. China. E-mail: 20231021@zzut.edu.cn

References

[1] Zhang C, Li N, Zhang P, Jiang Z, Cheng Y, Li H and Pang Z. Advancing precision and personalized breast cancer treatment through multi-omics technologies. Am J Cancer Res 2024; 14: 5614-5627.

[2] Bray F, Laversanne M, Sung H, Ferlay J, Siegel RL, Soerjomataram I and Jemal A. Global cancer statistics 2022: globocan estimates of incidence and mortality worldwide for 36 cancers in 185 countries. CA Cancer J Clin 2024; 74: 229-263.

[3] Ababneh E, Velez S and Zhao J. Immune evasion and resistance in breast cancer. Am J Cancer Res 2025; 15: 1517-1539.

[4] Taylor SR, Falcone JN, Cantley LC and Goncalves MD. Developing dietary interventions as therapy for cancer. Nat Rev Cancer 2022; 22: 452-466.

[5] Downer S, Berkowitz SA, Harlan TS, Olstad DL and Mozaffarian D. Food is medicine: actions to integrate food and nutrition into healthcare. BMJ 2020; 369: m2482.

[6] Hou Y and Jiang JG. Origin and concept of medicine food homology and its application in modern functional foods. Food Funct 2013; 4: 1727-1741.

[7] Lee YS, Kang J, Jung ES and Lee A. High expression of nrf2 and low expression of keap1 predict worse survival in patients with operable triple-negative breast cancer. J Breast Cancer 2023; 26: 461-478.

[8] Afzal F, Khalid W, Asif MN, Jabeen A, Jha RP, Khalid MZ, Fizza C, Aziz A, Akram R, Bashir A, Younas S, Nayyer F, Yasin R and Ahmad MZ. Role of mulberry leaves in human nutrition: a review. Acta Scientifci Nutritional Health 2021; 4: 43-50.

[9] Yu Y, Li H, Zhang B, Wang J, Shi X, Huang J, Yang J, Zhang Y and Deng Z. Nutritional and functional components of mulberry leaves from different varieties: evaluation of their potential as food materials. Int J Food Prop 2018; 21: 1495-1507.

[10] Ma Q, Li Y, Zhao R, Tang Z, Li J, Chen C, Liu X, Hu Y, Wang T and Zhao B. Therapeutic mechanisms of mulberry leaves in type 2 diabetes based on metabolomics. Front Pharmacol 2022; 13: 954477.

[11] Khakwani E, Rizwan B, Noreen S, Amjad A, Shehzadi M, Rashid N and Ijaz A. Functional and nutraceutical characterization of mulberry leaves. Pak Biomed J 2022; 5: 90-95.

[12] Buweialiye H, Guo L, Yue J, Jie R, Ding C and Wu G. Integrated network pharmacology and experimental validation reveal coreopsis tinctoria total flavonoids (ctfs) as potential therapeutic agents against hepatocellular carcinoma. Am J Cancer Res 2025; 15: 4639-4657.

[13] Zhao J, Han M, Nie Q, Wen X, Geng H, Zou Y, Li S and Xie W. Network pharmacology combined with experimental analysis to explore the mechanism of the xinshuaining formula on heart failure. 3 Biotech 2025; 15: 110.

[14] Ma G, Chai X, Hou G, Zhao F and Meng Q. Phytochemistry, bioactivities and future prospects of mulberry leaves: a review. Food Chem 2022; 372: 131335.

[15] Lv Q, Lin J, Wu X, Pu H, Guan Y, Xiao P, He C and Jiang B. Novel active compounds and the antidiabetic mechanism of mulberry leaves. Front Pharmacol 2022; 13: 986931.
[16] Li JS, Ji T, Su SL, Zhu Y, Chen XL, Shang EX, Guo S, Qian DW and Duan JA. Mulberry leaves ameliorate diabetes via regulating metabolic profiling and ages/rage and p38 mapk/nf-κb pathway. J Ethnopharmacol 2022; 283: 114713.
[17] Ru J, Li P, Wang J, Zhou W, Li B, Huang C, Li P, Guo Z, Tao W, Yang Y, Xu X, Li Y, Wang Y and Yang L. Tcmsp: a database of systems pharmacology for drug discovery from herbal medicines. J Cheminform 2014; 6: 13.
[18] Sherman BT, Hao M, Qiu J, Jiao X, Baseler MW, Lane HC, Imamichi T and Chang W. David: a web server for functional enrichment analysis and functional annotation of gene lists (2021 update). Nucleic Acids Res 2022; 50: W216-W221.
[19] Wang X, Zhang C, Liu L, Zhong Y, Wang Y, Liu F, Zhu J, Mu Z, Zhang S, Wang X, Zhong G, Liang J and Zeng J. Effective materials and mechanisms study of tibetan herbal medicine lagotis integra w. W. Smith treating dss-induced ulcerative colitis based on network pharmacology, molecular docking and experimental validation. J Ethnopharmacol 2023; 301: 115800.
[20] Eo HJ, Park JH, Park GH, Lee MH, Lee JR, Koo JS and Jeong JB. Anti-inflammatory and anticancer activity of mulberry (morus alba l.) Root bark. BMC Complement Altern Med 2014; 14: 200.
[21] Chan EW, Lye PY and Wong SK. Phytochemistry, pharmacology, and clinical trials of morus alba. Chin J Nat Med 2016; 14: 17-30.
[22] Khyade VB. Antioxidant activity and phenolic compounds of mulberry, morus alba (l) (variety: baramatiwali). J Med Plants Stud 2016; 4: 4-7.
[23] Maqsood M, Anam Saeed R, Sahar A and Khan MI. Mulberry plant as a source of functional food with therapeutic and nutritional applications: a review. J Food Biochem 2022; 46: e14263.
[24] Xu W, Gao Y, Wang Y and Guan J. Protein-protein interaction prediction based on ordinal regression and recurrent convolutional neural networks. BMC Bioinformatics 2021; 22 Suppl 6: 485.
[25] Dangroo NA, Rather MA, Singh J, Khursheed A, Mir JM and Shalla AH. Isolation and spectroscopic characterization of anticancer phytochemicals from artemisia laciniata: a combined experimental and theoretical investigation using admet analysis and in silico molecular docking simulation against key cancer targets. Nat Prod Res 2026: 40: 2168-2176.
[26] Wang Z, Zhang HM, Guo YR and Li LL. Molecular mechanisms of biyu decoction as treatment for psoriasis: a network pharmacology and molecular docking study. World J Clin Cases 2022; 10: 7224-7241.
[27] Zhuang Y, Ning C, Liu P, Zhao Y, Li Y, Ma Z, Shan L, Piao Y, Zhao P and Jin X. Lsm12 facilitates the progression of colorectal cancer by activating the wnt/ctnnb1 signaling pathway. Oncol Res 2022; 30: 289-300.
[28] Yan XT, Xu Y, Cheng XL, He XH, Wang Y, Zheng WZ, Zhao Y, Chen H and Wang YL. Sp1, MYC, CTNNB1, CREB1, JUN genes as potential therapy targets for neuropathic pain of brain. J Cell Physiol 2019; 234: 6688-6695.
[29] Tanabe S, Kawabata T, Aoyagi K, Yokozaki H and Sasaki H. Gene expression and pathway analysis of *CTNNB1* in cancer and stem cells. World J Stem Cells 2016; 8: 384-395.
[30] Deepa M, Sureshkumar T, Satheeshkumar PK and Priya S. Purified mulberry leaf lectin (mll) induces apoptosis and cell cycle arrest in human breast cancer and colon cancer cells. Chem Biol Interact 2012; 200: 38-44.
[31] Deepa M, Sureshkumar T, Satheeshkumar PK and Priya S. Antioxidant rich morus alba leaf extract induces apoptosis in human colon and breast cancer cells by the downregulation of nitric oxide produced by inducible nitric oxide synthase. Nutr Cancer 2013; 65: 305-310.
[32] Rauf A, Imran M, Khan IA, Ur-Rehman M, Gilani SA, Mehmood Z and Mubarak MS. Anticancer potential of quercetin: a comprehensive review. Phytother Res 2018; 32: 2109-2130.
[33] Liu X and Chen Z. Quercetin suppresses cell viability in triple-negative breast cancer by targeting ORM2. Am J Cancer Res 2024; 14: 5269-5285.
[34] Kaboli PJ, Imani S, Jomhori M and Ling KH. Chemoresistance in breast cancer: PI3K/AKT pathway inhibitors vs the current chemotherapy. Am J Cancer Res 2021; 11: 5155-5183.
[35] Yates ME, Waltermire H, Mori K, Li Z, Li Y, Guzolik H, Wang X, Liu T, Atkinson JM, Hooda J, Lee AV and Oesterreich S. *ESR1* fusions invoke breast cancer subtype-dependent enrichment of ligand-independent oncogenic signatures and phenotypes. Endocrinology 2024; 165: bqae111.
[36] Nagy Z and Jeselsohn R. ESR1 fusions and therapeutic resistance in metastatic breast cancer. Front Oncol 2023; 12: 1037531.
[37] Bahreini A, Li Z, Wang P, Levine KM, Tasdemir N, Cao L, Weir HM, Puhalla SL, Davidson NE, Stern AM, Chu D, Park BH, Lee AV and Oesterreich S. Mutation site and context dependent effects of ESR1 mutation in genome-edited breast cancer cell models. Breast Cancer Res 2017; 19: 60.

[38] Lei JT, Gou X and Ellis MJ. *ESR1* fusions drive endocrine therapy resistance and metastasis in breast cancer. Mol Cell Oncol 2018; 5: e1526005.
[39] XING X, LÜ D, CHAI Y and ZHU Z. Advances in the mechanism of traditional chinese medicine by network pharmacology method. Int J Pharm Pract 2018; 36: 97-102.
[40] Liang X, Pan Q, Liao Y, Nie L, Yang L, Liu F and Su M. In silico analysis and experimental validation to exhibit anti-nasopharyngeal carcinoma effects of plumbagin, an anti-cancer compound. J Sci Food Agric 2022; 102: 5460-5467.